PNAS RESEARCH ARTICLE | CHEMISTRY BIOCHEMISTRY

Elucidation of the tyrosinase/O_2/monophenol ternary intermediate that dictates the monooxygenation mechanism in melanin biosynthesis

Ioannis Kipouros[a], Agnieszka Stańczak[b,c], Jake W. Ginsbach[a], Prokopis C. Andrikopoulos[b,1], Lubomír Rulíšek[b,2], and Edward I. Solomon[a,d,2]

Edited by Michael Marletta, University of California, Berkeley, CA; received March 30, 2022; accepted July 5, 2022

Melanins are highly conjugated biopolymer pigments that provide photoprotection in a wide array of organisms, from bacteria to humans. The rate-limiting step in melanin biosynthesis, which is the *ortho*-hydroxylation of the amino acid L-tyrosine to L-DOPA, is catalyzed by the ubiquitous enzyme tyrosinase (Ty). Ty contains a coupled binuclear copper active site that binds O_2 to form a μ:η^2:η^2-peroxide dicopper(II) intermediate (oxy-Ty), capable of performing the regioselective monooxygenation of *para*-substituted monophenols to catechols. The mechanism of this critical monooxygenation reaction remains poorly understood despite extensive efforts. In this study, we have employed a combination of spectroscopic, kinetic, and computational methods to trap and characterize the elusive catalytic ternary intermediate (Ty/O_2/monophenol) under single-turnover conditions and obtain molecular-level mechanistic insights into its monooxygenation reactivity. Our experimental results, coupled with quantum-mechanics/molecular-mechanics calculations, reveal that the monophenol substrate docks in the active-site pocket of oxy-Ty fully protonated, without coordination to a copper or cleavage of the μ:η^2:η^2-peroxide O-O bond. Formation of this ternary intermediate involves the displacement of active-site water molecules by the substrate and replacement of their H bonds to the μ:η^2:η^2-peroxide by a single H bond from the substrate hydroxyl group. This H-bonding interaction in the ternary intermediate enables the unprecedented monooxygenation mechanism, where the μ-η^2:η^2-peroxide O-O bond is cleaved to accept the phenolic proton, followed by substrate phenolate coordination to a copper site concomitant with its aromatic *ortho*-hydroxylation by the non-protonated μ-oxo. This study provides insights into O_2 activation and reactivity by coupled binuclear copper active sites with fundamental implications in biocatalysis.

tyrosinase | binuclear copper | monooxygenase | oxygen activation | melanin biosynthesis

Biological pigmentation via the biosynthesis of small molecules and polymers is a widespread evolutionary adaptation found in a range of different environments (1). Melanins, a major class of highly conjugated biopolymer pigments, are essential for a diverse group of organisms, from soil bacteria to humans, due to their photoprotective, antioxidant, and metal-sequestering properties (2). The initial and rate-limiting step (RLS) in the biosynthesis of most melanins during melanogenesis, which is the O_2-dependent *ortho*-hydroxylation of the amino acid L-tyrosine to L-3,4-dihydroxyphenylalanine (L-DOPA), as well as the subsequent two-electron oxidation of L-DOPA to L-DOPAquinone (Fig. 1*A*), are both catalyzed by the same ubiquitous enzyme tyrosinase (Ty) (3). Due to its key catalytic role in both microbial and mammalian melanogenesis, Ty has become an emerging therapeutic target for the treatment of bacterial and fungal infections (4), as well as for the early detection, prevention, and treatment of complex human diseases, including skin cancer (5, 6) and Parkinson's disease (7, 8). The direct link between melanogenesis and fruit browning has also made plant Ty, as well as the phylogenetically related catechol oxidases (CaOxs), critical agrotechnological targets toward improving food quality and extending produce shelf life (9). Beyond its role in melanin biosynthesis, the high regioselectivity and broad substrate promiscuity toward the aromatic monooxygenation of a range of *para*-substituted monophenols has made Ty a promising enzymatic tool for a number of challenging chemical transformations and biotechnological applications, including protein bioconjugation (10), bioorthogonal chemistry (11), metabolite biosensors (12, 13), and bioremediation (14). However, advancements in these key areas and a fundamental molecular-level understanding of melanogenesis are limited by the lack of detailed mechanistic insights into the enzymatic monooxygenation reaction.

Previous crystallographic and spectroscopic studies have shown that the reactivity of Ty is afforded by its coupled binuclear copper (CBC) active site, where a conserved four-alpha-helix bundle brings two Cu ions, each coordinated by three histidine

Significance

Melanins are ubiquitous photoprotective biopolymer pigments with major implications ranging from fruit browning to severe human diseases, including skin cancer. Tyrosinase, the enzyme catalyzing the rate-limiting step in melanin biosynthesis is thus an important biotechnological and therapeutic target. Tyrosinase contains a coupled binuclear copper active site that binds dioxygen to form a μ-η^2:η^2-peroxide dicopper(II) intermediate (oxy-tyrosinase) which is activated toward the regioselective aromatic monooxygenation of *para*-substituted monophenols via a poorly defined mechanism. Here, we have employed spectroscopic, kinetic, and computational methods to trap and characterize the elusive catalytic ternary intermediate formed upon monophenol binding to oxy-tyrosinase and elucidate the mechanism of the subsequent monooxygenation reaction. This study provides unprecedented molecular-level insights into the rate-limiting step in melanin biosynthesis.

The authors declare no competing interest.

This article is a PNAS Direct Submission.

[1]Present address: Institute of Biotechnology, Czech Academy of Sciences, 252 50 Vestec, Czech Republic.

[2]To whom correspondence may be addressed. Email: solomone@stanford.edu or lubomir.rulisek@uochb.cas.cz.

This article contains supporting information online at http://www.pnas.org/lookup/suppl/doi:10.1073/pnas.2205619119/-/DCSupplemental.

Published August 8, 2022.

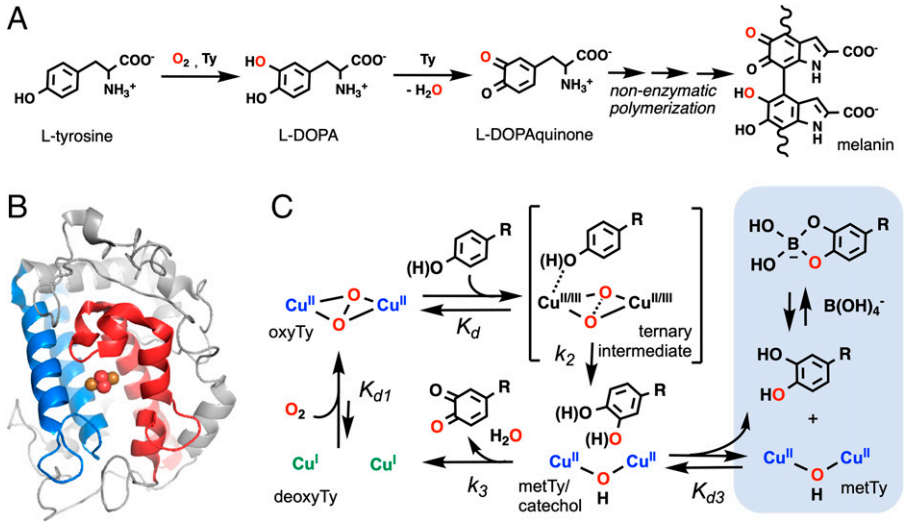

Fig. 1. (*A*) The rate-limiting monooxygenation step of L-tyrosine to L-DOPA and the subsequent oxidation of L-DOPA to L-DOPAquinone in melanin biosynthesis are both catalyzed by Ty. (*B*) Structure of oxy-Ty from *S. castaneoglobisporous* (PDB: 1WX2) (15), with the four-alpha-helix bundle shown in blue and red and each color corresponding to their respective coordination of Cu_A and Cu_B (Cu, brown spheres; μ-η^2:η^2-peroxide, red spheres). (*C*) Kinetic scheme for the catalytic cycle (monophenol monooxygenation and catechol oxidation reactions) of Ty toward *para*-substituted monophenols, with the effect of borate trapping the catechol product shown in the shaded region. The elusive ternary intermediate is shown in brackets. For the extended kinetic scheme, see *SI Appendix*, Scheme S1.

residues, in close proximity to each other (<5 Å; Fig. 1*B*) (3). During the catalytic cycle, the μ-hydroxo dicopper(II) active site of the resting enzyme (met-Ty) oxidizes catechols to *ortho*-quinones and is reduced to its dicopper(I) state (deoxy-Ty), which then reversibly binds molecular dioxygen to form a μ-η^2:η^2-peroxide dicopper(II) intermediate (oxy-Ty) that possesses both monophenol monooxygenation and catechol oxidation reactivities (Fig. 1*C*, unshaded region) (3). All catalytic forms of Ty are diamagnetic, which in the cases of met-Ty and oxy-Ty is due to the strong antiferromagnetic coupling of their two Cu(II) centers afforded by their bridging ligands (3). Similar to the oxy-intermediates of other CBC proteins, oxy-Ty exhibits distinct electronic absorption bands (ε_{345nm} ~16,000 cm^{-1} M^{-1}, ε_{650nm} ~1,000 cm^{-1} M^{-1}) and resonance Raman (rR) features (section 2.3), reflecting its unique electronic structure, where the strong donor interactions of the side-on peroxide with both Cu(II) centers result in its intense high-energy charge-transfer (CT) band (16), while the back-bonding interaction with the μ-η^2:η^2-peroxide is responsible for its relatively low O-O stretching frequency (~740 cm^{-1}) (17).

While oxy-Ty unambiguously has a μ-η^2:η^2-peroxide dicopper(II) active site (3), model complex studies have demonstrated that such species can be in an equilibrium with their bis-μ-oxo dicopper(III) electronic isomers (18), both of which are able to monooxygenate phenolates to their corresponding catechol products. In some reported cases, μ-η^2:η^2-peroxide $Cu^{II}_2O_2$ model complexes can directly monooxygenate aromatic substrates without substrate coordination (19), while in others, phenolate coordination to one of the Cu centers promotes the cleavage of the μ-η^2:η^2-peroxide O-O bond to form a bis-μ-oxo $Cu^{III}_2O_2$ core before substrate monooxygenation (20). The enzymatic monooxygenation reaction mechanism is similarly expected to be dictated by the geometric and electronic structure of the Cu_2O_2 core in the ternary (Ty/O_2/monophenol) intermediate, which is formed upon the binding of the monophenol or monophenolate substrate to the oxy-Ty active site. However, this ternary intermediate remains elusive, despite previous efforts (21). In addition, given that under the typical range of physiological conditions for melanin biosynthesis (pH 4 to 7), the native substrate, L-tyrosine (pK_a = 10), is predominantly in its fully protonated monophenolic form (3), the protonation state of the substrate during its binding to oxy-Ty and the identity of the putative phenolic proton acceptor site in the ternary intermediate remain subjects of debate (22–26). Consequently, the lack of critical experimental evidence on the nature of the catalytic ternary intermediate of Ty significantly limits our mechanistic understanding of its monooxygenation reactivity toward monophenols.

In this study, we use a *para*-substituted monophenol substrate that exhibits both sufficient binding to oxy-Ty and slow subsequent monooxygenation to trap and spectroscopically (optical absorption and rR) characterize the catalytic ternary intermediate of Ty from *Streptomyces glaucescens* under single-turnover conditions and obtain key mechanistic insights into its subsequent monooxygenation reaction. Our experimental data, coupled with quantum-mechanics/molecular-mechanics (QM/MM) calculations, indicate that the monophenolic substrate binds to the active-site pocket of oxy-Ty fully protonated, without cleavage of the μ-η^2:η^2-peroxide O-O bond and without direct coordination to a Cu center. Formation of this ternary intermediate involves the displacement of the recently reported active-site water molecules (27), and replacement of their H-bonding interactions with the μ-η^2:η^2-peroxide by a single H bond from the hydroxyl group of the docked full-protonated monophenol substrate. This unprecedented substrate binding mode to a μ-η^2:η^2-peroxide dicopper(II) active site has direct mechanistic implications. Indeed, further investigations into the reactivity of this ternary intermediate reveal the key steps of the monooxygenation mechanism of Ty, where enabled by its H-bonding interaction with the substrate, the μ-η^2:η^2-peroxide O-O bond breaks to accept the phenolic $H^{+/\bullet}$. This step is followed by monophenolate substrate coordination to a Cu center concomitant with its aromatic *ortho*-hydroxylation by the nonprotonated μ-oxo. Overall, this study defines the mechanism of the critical monooxygenation reaction in melanin biosynthesis and provides a unifying mechanistic framework for the diverse Cu_2O_2 chemistry of model complexes and biological active sites.

2. Results and Analysis

2.1. Uncoupling the monophenol monooxygenation and catechol oxidation reactions. In order to directly probe the monophenol monooxygenation reaction of oxy-Ty, we proceeded to uncouple it from its subsequent catechol oxidation reaction that completes the catalytic cycle. To this end, we employed a previously reported borate system (28), where the catechol product of the monooxygenation reaction dissociates from the met-Ty active site before its further oxidation to *ortho*-quinone and is trapped by its condensation-driven complexation with borate (Fig. 1*C*, shaded region). Under these conditions, and in the absence of any external reductants, the monooxygenation of monophenols by oxy-Ty would be converted into a single-turnover reaction. This approach was evaluated by monitoring the time course for the reaction of oxy-Ty with a series of *para*-substituted monophenols via measuring O_2 consumption (*SI Appendix*, section 2.1.1) and product formation (*SI Appendix*, section 2.1.2). The reactions of oxy-Ty with monophenols containing electron-donating *para* groups result in the consumption of multiple O_2 equivalents (*SI Appendix*, Fig. S2 *A–D*) and the generation of their respective quinone products (*SI Appendix*, Fig. S4 *A–D*), indicating that these are in fact multiple turnover reactions. However, the reactions of oxy-Ty with the two monophenols containing electron-withdrawing *para* groups, 4-hydroxybenzamide (4-$CONH_2$) and methyl 4-hydroxybenzoate (4-$COOCH_3$), result in neither the consumption of additional O_2 equivalents (*SI Appendix*, Fig. S2 *E* and *F*) nor the generation of their chromophoric quinone and further oxidation products, indicating that these are indeed single-turnover reactions (*SI Appendix*, Fig. S4*E* and Fig. 2*A*).

The above results indicate that the single-turnover efficiency of the borate-based kinetic scheme (Fig. 1*C*) is substrate dependent and can be rationalized in terms of distinct *para*-group effects. First, the inductive and resonance *para*-group effects dictate the two-electron reduction potential of the *para*-substituted quinone products, with more electron-withdrawing *para* groups slowing down the rate of catechol oxidation to *ortho*-quinone by met-Ty (k_3). Second, the binding affinity of the catechol product to the met-Ty active site is expected to vary with different *para* groups and thus affect the extent of catechol dissociation (K_{d3}). Finally, the competitive inhibition of the generated met-Ty by the high excess of the *para*-substituted monophenolic substrate (K_{i1} in *SI Appendix*, Scheme S1) (29) is similarly expected to vary with *para* group and thus suppress multiple turnovers to different extents. Importantly, the reactions of oxy-Ty with the monophenols 4-$CONH_2$ and 4-$COOCH_3$ exhibit complete uncoupling of the timescales for their monooxygenation and catechol oxidation reactions, providing the opportunity to study the monooxygenation reaction of Ty under single-turnover conditions.

2.2. Formation and reactivity of the ternary intermediate. To investigate the possible formation of the elusive ternary intermediate (Ty/O_2/monophenol), the single-turnover reaction of oxy-Ty with the 4-$COOCH_3$ substrate was monitored by stopped-flow absorption (SF-Abs) spectroscopy after mixing deoxy-Ty with increasing substrate concentrations in O_2-saturated borate buffer (parallel kinetic investigations for the 4-$CONH_2$ substrate yielded equivalent results; *SI Appendix*, section 2.2.1). For all 4-$COOCH_3$ concentrations, the instantaneous appearance of the two absorption bands at 345 and 650 nm, corresponding to the two characteristic peroxide→Cu(II) CT transitions of the μ-η^2:η^2-peroxide dicopper(II) active site, indicates fast and exergonic O_2 binding in deoxy-Ty to form oxy-Ty. These absorption bands subsequently undergo first-order exponential decay at a rate accelerated with increasing substrate concentration and notably without the prior or concomitant formation of anyabsorption features (Fig. 2*A*). The rate constants (k_{obs}) obtained by fitting the decay of the 350-nm traces (Fig. 2*A*, insert) exhibit linear dependence at lower substrate concentrations and progressive saturation at increasing substrate concentrations (Fig. 2*B*). Under our single-turnover conditions, this nonlinear dependence of the k_{obs} values over increasing substrate concentration requires our kinetic scheme to include the ternary intermediate (Ty/O_2/4-$COOCH_3$) that forms via the fast and reversible binding of the monophenolic substrate to oxy-Ty (K_d = 13 mM; Fig. 1*C*) and decays via the slow and irreversible monooxygenation reaction to form the catechol product (k_2 = 0.56 s^{-1}; Fig. 1*C*). The fast and reversible binding (k_{on}) and dissociation (k_{off}) of the monophenolic substrate to oxy-Ty is supported by the substrate concentration-dependent saturation of k_{obs}, which requires $k_{on} \gg k_2$ and is confirmed by spectroscopic characterization of an early-time (100 ms) reaction mixture by rR spectroscopy (section 2.3). Note also that binding of the monophenol substrate to deoxy-Ty (29), which can slow or prevent subsequent binding of O_2, is found not to be significant for the 4-$COOCH_3$ substrate under the high postmixing O_2 concentrations (>1 mM) employed in our experiments (*SI Appendix*, Fig. S8).

Based on the obtained kinetic parameters for the formation (K_d) and decay (k_2) of the ternary intermediate, at early times (100 ms) and at the highest 4-$COOCH_3$ concentrations (10 mM postmixing, solubility limited), the ternary intermediate accumulates at ∼43% of the total enzyme concentration. Using this early-time speciation, the UV-vis absorption spectrum of the ternary intermediate can be obtained from the 100-ms SF-Abs spectrum for the reaction of deoxy-Ty with an O_2-saturated solution of 4-$COOCH_3$ (10 mM), after correction for the spectral contributions from oxy-Ty and intensity renormalization. The resulting ultraviolet-to-visible (UV-vis) absorption spectrum for the ternary intermediate exhibits two absorption bands with energies and intensities similar to those corresponding to the two peroxide→Cu(II) CT transitions in oxy-Ty (Fig. 2*C*), indicating that the ternary intermediate also contains a similar μ-η^2:η^2-peroxide dicopper(II) active site. Note that unlike previous proposals from model complex studies (20), our results do not support the possibility of a substrate-coordinated bis-μ-oxo dicopper(III) active site in the ternary intermediate of Ty, as none of the characteristic absorption features for the oxo→Cu(III) and phenolate→Cu(III) CT transitions in the 350- to 550-nm region are observed (21, 30).

To determine the protonation state of the 4-$COOCH_3$ substrate (i.e., monophenol versus monophenolate) during the formation of the ternary intermediate, the pH dependence of its reaction with oxy-Ty was evaluated by SF-Abs kinetic experiments. Our results show that while k_2 is pH independent, the apparent K_d decreases with decreasing pH (*SI Appendix*, Fig. S7*A*), indicating that the monophenolic form of 4-$COOCH_3$ binds to oxy-Ty more favorably than its monophenolate form. Together, our above results clearly demonstrate that the ternary intermediate contains a μ-η^2:η^2-peroxide dicopper(II) core with the substrate bound at the active site as either 1) a monophenol or 2) a monophenolate with its phenolic proton accepted by an active-site base. Further insights into the identity of the proton acceptor site and the interactions between the bound substrate and the $Cu(II)_2O_2$ core in the ternary intermediate were obtained by higher-resolution spectroscopic investigations (section 2.3).

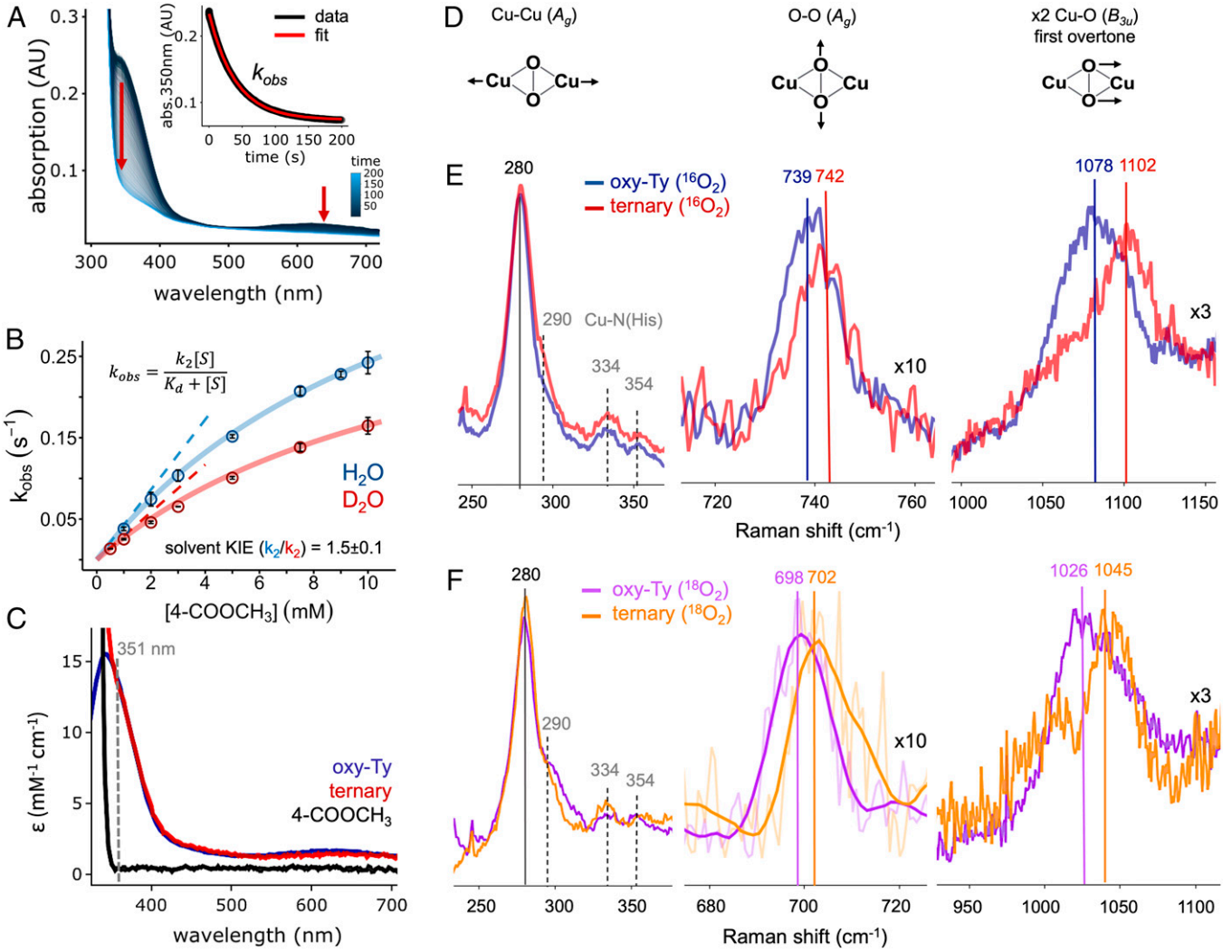

Fig. 2. Kinetic and spectroscopic definition of the ternary intermediate (Ty/O_2/4-$COOCH_3$). (*A*) SF-Abs spectra of the reaction of oxy-Ty (20 μM) with 4-$COOCH_3$ (1 mM) in O_2-saturated borate buffer (pH 9.0, 4 °C, 10% ethylene glycol). Insert: 350 nm absorption (abs) trace with first-order decay fit (AU; absorbance units). (*B*) Dependence of k_{obs} on 4-$COOCH_3$ concentration in H_2O (blue) and D_2O (red) with saturation fits for a fast equilibrium, followed by a slow irreversible step (equation shown as insert, complete model fits shown as solid lines, and linear fits for low substrate concentrations shown as dashed lines; error bars denote standard deviations for n = 3). (*C*) UV-vis absorption spectra for the ternary intermediate (red), oxy-Ty (blue), and 4-$COOCH_3$ (black), with the excitation wavelength for rR (351 nm) indicated as a dashed gray line. (*D*) The main vibrational modes of the $Cu^{II}_2O_2$ core (D_{2h}) that are resonance enhanced with excitation of the peroxide(π^*_σ)→Cu^{II} CT. (*E* and *F*) rR spectra (351-nm laser excitation) of oxy-Ty and the ternary intermediate (Ty/O_2/4-$COOCH_3$) in (*E*) $^{16}O_2$ and (*F*) $^{18}O_2$, with the relative intensity of each region scaled as indicated. Solid vertical lines indicate the energies of the main vibrational modes and dashed gray lines the Cu-N(His) modes. The oxy-Ty and the ternary intermediate samples were obtained by RFQ (100 ms) after 1:1 mixing of deoxy-Ty (0.8 mM) and an O_2-saturated solution of borate buffer (pH 9.0, 4 °C, 10% ethylene glycol) without or with 4-$COOCH_3$ (20 mM), respectively. The rR spectra were obtained after correction for background contributions, with the spectrum of the pure ternary intermediate obtained by further correcting for the oxy-Ty contributions in the RFQ reaction mixture and subsequent intensity renormalization. Due to experimental limitations resulting in lower $^{18}O_2$ concentrations in *F* (*SI Appendix, Materials and Methods*, section 1.1.9), additional first- and second-order polynomial baseline corrections were applied for the 680- to 720- and 950- to 1,100-cm^{-1} regions, respectively, with a smoothened spectrum also included in the 680- to 720-cm^{-1} region. The $^{16/18}O_2$ rR spectra, without smoothening, are shown in *SI Appendix*, Fig. S11.

Our single-turnover SF-Abs experiments also allowed investigations of the reactivity of the ternary intermediate by probing the monooxygenation step (k_2) following the binding of the monophenol substrate to oxy-Ty. First, upon solvent isotopic substitution (H_2O/D_2O), the reaction of deoxy-Ty with 4-$COOCH_3$ in O_2-saturated borate buffer exhibits a small normal solvent kinetic isotope effect (KIE) of 1.5 ± 0.1 on k_2 (Fig. 2*B*). Since the geometric structure of the oxy-Ty active site is not perturbed upon solvent deuteration (27), the observed solvent KIE likely reflects the participation of one or more exchangeable protons in the transition state (TS) of the RLS, clearly implicating the phenolic substrate proton in the monooxygenation reaction mechanism. This is fully consistent with our pH dependence results (*SI Appendix*, Fig. S7*A*), demonstrating that the substrate binds to oxy-Ty as a monophenol, and further suggests that the bound substrate remains fully protonated in the ternary intermediate. Second, the reaction of oxy-Ty with the dideuterated (in both *ortho* positions to the hydroxy group) 4-$COOCH_3$ substrate does not exhibit an inverse secondary KIE on k_2 (or an equilibrium isotope effect on K_d; *SI Appendix*, Fig. S7*C*) indicating that in the TS of the RLS, the *ortho*-C center (to be hydroxylated) retains a significant amount of its sp^2 character, since a small inverse KIE is expected for a fully C(sp^3) TS (30). Third, the Eyring plot for the temperature dependence of k_2 in the reaction of oxy-Ty with 4-$COOCH_3$ provides the enthalpic ($\Delta H^{\ddagger}$ = +10.3 ± 0.7 kcal/mol) and entropic ($\Delta S^{\ddagger}$ = −0.023 ± 0.003 kcal/mol*K) components of the RLS in the monooxygenation reaction (*SI Appendix*, Fig. S7*B*).

2.3. Spectroscopic definition of the ternary intermediate. Both oxy-Ty and the ternary intermediate (Ty/O_2/4-$COOCH_3$) were trapped at ~100 ms by rapid-freeze quench (RFQ) after 1:1 mixing of deoxy-Ty (0.8 mM) with an O_2-saturated buffer solution (0.5 M borate, pH 9.0, 4 °C) without and with 4-$COOCH_3$ (10 mM), respectively, and their rR spectra were collected with 351-nm laser excitation into their high-energy peroxide(π^*_σ)→Cu^{II} CT band (Fig. 2*C*). The rR spectrum of oxy-Ty exhibited the characteristic resonance-enhanced peaks associated with the μ-η^2:η^2-peroxide dicopper(II) vibrational modes (Fig. 2 *D*; blue/purple spectra in Fig. 2 *E* and *F* and Figs. S9*A* and S11) (31). These modes include 1) the Cu-Cu (A_g) stretch at 280 cm^{-1} ($\Delta^{18}O_2 < -2$ cm^{-1}), 2) the weak Cu-N(His) modes in the 290- to 360-cm^{-1} region ($\Delta^{18}O_2 < -2$ cm^{-1}), 3) the peroxide O-O (A_g) stretch at 739 cm^{-1} ($\Delta^{18}O_2 = -40$ cm^{-1}), and 4) the intense first overtone of the Cu-O (B_{3u}) mode at 1,078 cm^{-1} ($\Delta^{18}O_2 = -51$ cm^{-1}), which is allowed and present at double the frequency of its corresponding weak fundamental mode, which is nontotally symmetric and thus rR forbidden.

The rR spectrum for the RFQ 100-ms reaction mixture of oxy-Ty (57%) and the ternary intermediate (43%) also exhibits the characteristic peaks for a μ-η^2:η^2-peroxide dicopper(II) active site (*SI Appendix*, Fig. S9*A*). Importantly, the normalized peak intensity of the O-O (A_g) stretch (using the nearby borate peak at 920 cm^{-1} as an internal standard) in the oxy-Ty (57%)/ternary intermediate (43%) mixture is equivalent to that of oxy-Ty (100%), further confirming our SF-Abs results that the ternary intermediate contains a μ-η^2:η^2-peroxide dicopper(II) active site (*SI Appendix*, Fig. S9*A*, insert). Comparison between the corrected (for baseline, buffer, and speciation) and intensity-renormalized rR spectra of oxy-Ty and the ternary intermediate reveals the spectral changes due to interactions between the μ-η^2:η^2-peroxide dicopper(II) core and the bound substrate (Fig. 2 *E* and *F* and *SI Appendix*, Fig. S9). These include 1) a 3 ± 2 cm^{-1} increase of the O-O (A_g) stretch; 2) a 24 ± 6 cm^{-1} increase of the first overtone of the Cu-O (B_{3u}) stretch, indicating a 12 ± 3 cm^{-1} increase in the corresponding fundamental mode; and 3) no significant change (<±2 cm^{-1}) in the Cu-Cu and Cu-N(His) modes. Note that upon solvent deuteration and within our signal-to-noise ratio, no significant perturbations (>±6 cm^{-1}) in the rR mode frequencies for the ternary intermediate were resolved (*SI Appendix*, Fig. S12). Together, our spectroscopic results demonstrate that the electronic/geometric structure of the μ-η^2:η^2-peroxide dicopper(II) site in oxy-Ty is only moderately perturbed upon binding of the monophenol substrate to form the ternary intermediate.

2.4. Correlation of spectroscopic data to QM/MM models: Geometric and electronic structure of the ternary intermediate. To elucidate the geometric and electronic structure of the ternary intermediate, our spectroscopic results (sections 2.2 and 2.3) were correlated to QM/MM calculations. We have recently reported the experimentally calibrated, QM/MM-optimized structure of oxy-Ty from *Streptomyces castaneoglobisporous* (Fig. 1*B*; 100% active-site homology with *S. glaucescens*), which contains H-bonding

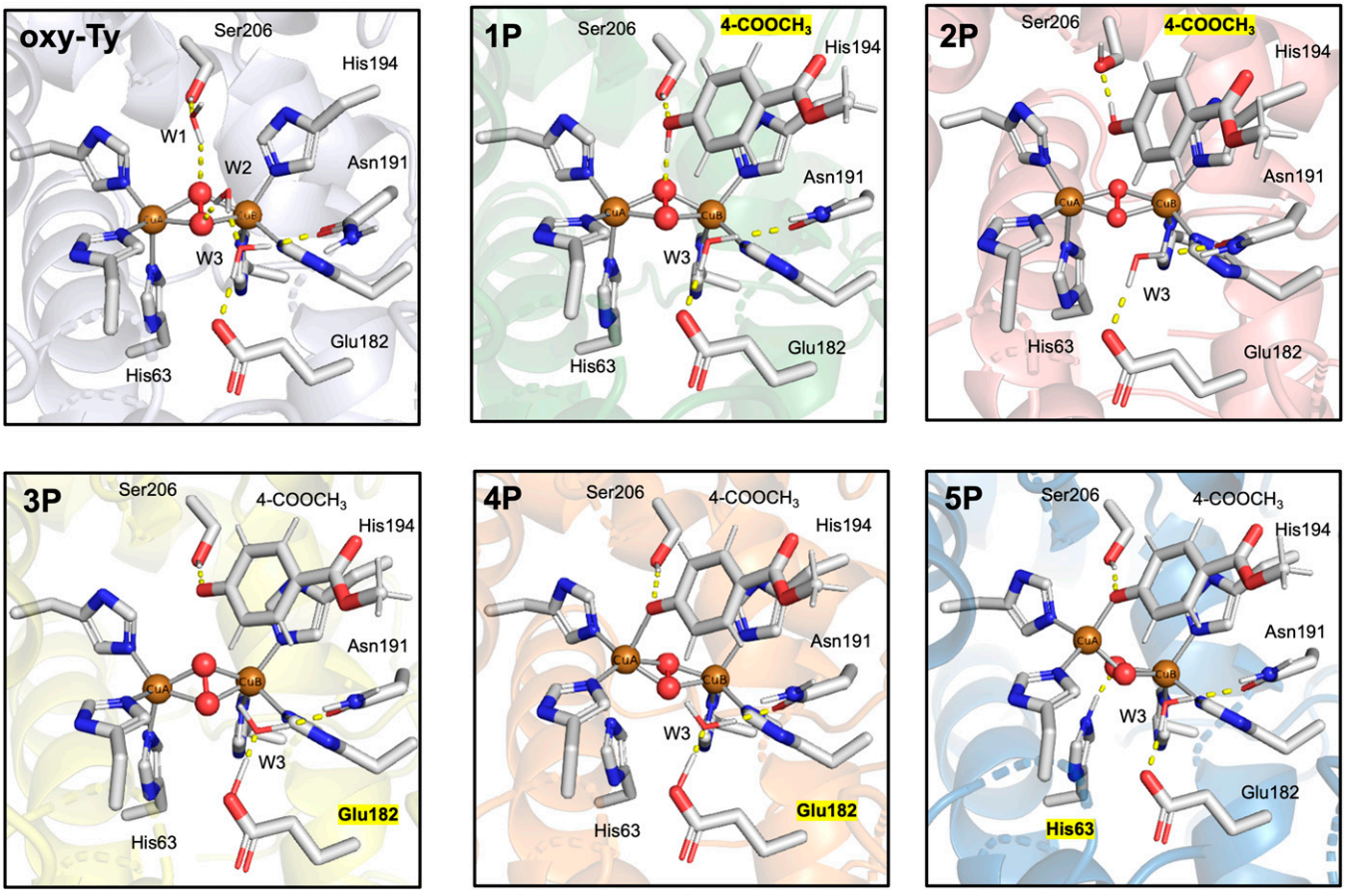

Fig. 3. The active sites of the QM/MM-optimized structures of oxy-Ty in *S. castaneoglobisporous* and its possible ternary intermediates (Ty/O_2/4-$COOCH_3$; 1P to 5P). Key active-site residues and the bound substrate (4-$COOCH_3$) are shown as sticks, the Cu sites and the μ-η^2:η^2-peroxide atoms are shown as spheres, the Cu coordination bonds are shown as solid gray lines, and H-bonding interactions are shown as dashed yellow lines. The label of the phenolic proton site in each ternary structure is highlighted in yellow. Equivalent structures for the possible ternary intermediates with the native substrate, L-tyrosine, are shown in *SI Appendix*, Fig. S15.

interactions between conserved active-site water molecules (W1 and W2) and the μ-η^2:η^2-peroxide (oxy-Ty in Fig. 3) (27). This oxy-Ty structure was employed as both the reference for the oxy-Ty active site and the starting point to generate a series of distinct QM/MM-optimized structures for possible ternary intermediates containing a μ-η^2:η^2-peroxide dicopper(II) active site (1P to 5P in Fig. 3). These ternary structures include, to the best of our knowledge, all those proposed in previous enzymatic and model complex studies (21, 24, 32) and were generated by systematically evaluating all reasonable possibilities involving the phenolic proton acceptor site, including the nearby Glu182/Asn191/W3 site (3P to 4P in Fig. 3) and the axial His63 ligand (5P in Fig. 3), as well as the possibility that the phenolic proton remains on the bound substrate (1P to 2P in Fig. 3 and 6P in *SI Appendix*, Fig. S17). For each of these possibilities, we also considered whether or not the substrate coordinates to Cu_A (i.e., the Cu coordinated by His residues closer to the N terminus; 3P versus 4P to 5P and 1P to 2P versus 6P in Fig. 3 and *SI Appendix*, Fig. S16; note that 6P requires fixed $O_{substrate}$-Cu_A coordination to obtain an optimized structure and relaxes to 1P when the constraint is removed). Finally, in the case where the substrate binds protonated as a monophenol, we further considered the possibility that it can H bond to the μ-η^2:η^2-peroxide via its hydroxyl group (1P versus 2P in Fig. 3). This approach allowed us to compile a comprehensive set of all reasonable structures for the ternary intermediate. Common in all of our QM/MM-optimized ternary structures is that the substrate is docked in the active-site pocket via π-π stacking interactions with His194 of Cu_B (i.e., the Cu coordinated by His residues closer to the C terminus), consistent with the previously reported Ty crystal structures with L-tyrosine bound to Zn-substituted and caddie-bound Ty crystal structures (15, 22).

The calculated changes in the electronic absorption and vibrational frequencies for the possible ternary intermediates (1P to 5P) relative to the oxy-Ty reference are summarized in Table 1. First, QM-frequency calculations for the ternary intermediate structures with the bound monophenolate substrate coordinated to Cu_A or the substrate phenolic proton transferred to either the nearby conserved Glu182 (4P in Fig. 3) or the now-dissociated axial His63 ligand of Cu_A (5P in Fig. 3), respectively, show either a large increase in the Cu-O stretch (+81 cm^{-1}; 4P) or a large decrease in the O-O stretch (−50 cm^{-1}; 5P), both inconsistent with our rR results. In addition, time-dependent density functional theory (TD-DFT) calculations show that the absorption spectra for both 4P and 5P would exhibit significant differences from that of oxy-Ty (*SI Appendix*, Fig. S14). Similarly, for the ternary intermediate structure with the bound monophenolate substrate not coordinated to a metal site and with its phenolic proton transferred to Glu182 (3P in Fig. 3), QM-frequency calculations predict a large increase of the O-O frequency (+24 cm^{-1}) and TD-DFT calculations indicate a decrease in the energy of the intense high-energy absorption band (+30 nm), both inconsistent with our experimental results. However, formation of the ternary intermediate by docking of the substrate protonated, noncoordinated to Cu_A, and H-bonded to the μ-η^2:η^2-peroxide (1P) most closely reproduces both the observed UV-vis absorption (*SI Appendix*, Fig. S14) and the rR spectra (along with their $^{16/18}O_2$ and H_2O/D_2O perturbations; Table 1) and is the most thermodynamically stable structure among the possible ternary intermediates in Table 1. Note that removal of the H-bonding interaction between the hydroxyl group of the bound substrate and the μ-η^2:η^2-peroxide in 1P (resulting in 2P in Fig. 3) results in QM-frequency changes that no longer reproduce our rR (Table 1) and UV-vis absorption results (*SI Appendix*, Fig. S14), while the thermodynamic energy increases by +5 kcal/mol. In addition, even when considering each of the 63 distinct structures for the oxy-Ty active site (with various active-site hydration levels, number/strength of water H bonds to the μ-η^2:η^2-peroxide, and thermodynamic stabilities) that we had previously evaluated toward defining the oxy-Ty structure shown in Fig. 3 (27), none of the 2P to 5P ternary structures can reproduce the observed O-O (A_g) and Cu-O (B_{3u}) vibrational perturbations (*SI Appendix*, Fig. S13).

Overall, our experimentally supported QM/MM model defines the electronic and geometric structure of the elusive catalytic ternary intermediate of Ty (1P in Fig. 3). Importantly, upon substrate binding to the oxy-Ty active site, the two conserved water molecules (W1 and W2 in oxy-Ty in Fig. 3) are displaced, and their direct H-bonding interactions with the μ-η^2:η^2-peroxide ($r[O_{W1}\text{-}O_1]$ = 3.1 Å, $r[O_{W2}\text{-}O_2]$ = 2.8 Å) are replaced by a single moderate H bond from the hydroxyl group ($r[O_{substrate}\text{-}O_1]$ = 2.7 Å). The mechanistic implications to the monooxygenation reaction that arise from this unprecedented substrate binding mode in 1P and its H-bonding interaction to the μ-η^2:η^2-peroxide are explored below.

2.5. Mechanistic insights into the monooxygenation reaction from experimentally supported QM/MM calculations. While the complete reaction coordinate of Ty will be the subject of a future study, here we provide mechanistic insights into the two key steps of the monooxygenation reaction. To this end, we

Table 1. Summary for the correlation of experimental with computational results for the possible ternary (Ty/O_2/4-$COOCH_3$) intermediates from Fig. 3.

	Frequency changes for key Cu_2O_2 vibrational modes (cm^{-1})						Same UV-vis abs. spectra for ternary and oxy-Ty*	Relative energy† (kcal/mol)
	Δ(ternary-oxy-Ty)			Ternary Δ($^{18}O_2$-$^{16}O_2$)/Δ(D_2O-H_2O)				
	Cu-Cu (A_g)	Cu-O (B_{3u})	O-O (A_g)	Cu-Cu (A_g)	Cu-O (B_{3u})	O-O (A_g)		
Exp.	0 ± 2	+12 ± 3	+3 ± 2	0 ± 2/0 ± 2	−29 ± 6/0 ± 6	−40 ± 2/0 ± 2	yes	—
1P	+11	+18	−3	−2/0	−20/−2	−50/−1	yes	0.0
2P	+24	+69	−5	−1/0	−15/+6	−49/−1	no	+5.1
3P	+21	−2	+24	−5/0	−19/0	−50/0	no	+21.4
4P	+18	+81	−13	−4/0	−21/0	−49/0	no	+22.5
5P	+21	+25	−50	−6/0	−21/−3	−43/+1	no	+8.1

Exp, denotes experimental values and abs, UV-Vis absorption.
*For 1P to 5P, the TD-DFT spectra are shown in *SI Appendix*, Fig. S14.
†QM-only energy upon QM/MM-optimized geometries using the TPSS/def2-TZVPD level of theory in the homogeneous dielectric continuum with $\varepsilon_r = 8$.

correlated our experimental data on the monooxygenation reaction to QM/MM and QM-only (i.e., QM-cluster calculations on top of the QM/MM-optimized structures) calculations to evaluate the reaction steps following the formation of the ternary intermediate (Ty/O_2/4-$COOCH_3$) and toward the aromatic *ortho*-hydroxylation of the bound substrate. Starting from the newly defined structure of 1P (Fig. 3), we systematically assessed reaction steps by obtaining intermediates and their corresponding TSs along 1) O-O bond cleavage of the μ-η^2:η^2-peroxide, 2) substrate deprotonation via cleavage of its O-H bond, 3) substrate monooxygenation via C_{ortho}-O bond formation, and 4) substrate coordination via Cu_A-$O_{substrate}$ bond formation.

Direct *ortho*-hydroxylation of the protonated substrate in 1P by the μ-η^2:η^2-peroxide or bis-μ-oxo (after O-O cleavage) exhibit high-energy barriers (>25 kcal/mol, *SI Appendix*, Fig. S16), indicating that the hydroxylation step must be preceded by deprotonation of the bound substrate. While in section 2.4 (and *SI Appendix*, section 2.5.2) we determined that the previously proposed proton-acceptor active-site residues show low basicity (Glu182/Asn191/W3 for 3P and His63 for 4P in Fig. 3, Table 1, and *SI Appendix*, section 2.5.2), the Cu_2O_2 core is a plausible H-acceptor site, particularly in its bis-μ-oxo form. Indeed, a two-dimensional (2D) scan along the cleavage of both the peroxide O-O and the substrate O-H bonds (Fig. 4*B*) shows a low TS barrier (+7.0 kcal/mol) for O-O cleavage, enabling fast H^+ transfer (along with 0.6 electron spin density; *SI Appendix*, Table S2) to form a μ-oxo-μ-hydroxo dicopper intermediate (2O in Fig. 4*A*) of reasonable thermodynamic stability (+1.5 kcal/mol). Comparison of the QM/MM reaction coordinates between 1P and 2P reveals that the H-bonding interaction between the substrate hydroxyl group and the μ-η^2:η^2-peroxide in 1P stabilizes not only the reactant state (by +5.1 kcal/mol) but also the resulting 2O intermediate (by +7 kcal/mol; *SI Appendix*, Fig. S18). Thus, in the ternary intermediate, the H-bonding interaction between the protonated substrate and the μ-η^2:η^2-peroxide enables the efficient cleavage of the μ-η^2:η^2-peroxide O-O bond and enhances $H^{+/\bullet}$ transfer to the Cu_2O_2 core, making the resulting 2O intermediate thermodynamically accessible.

In 2O, the substrate *ortho*-C is oriented toward the nonprotonated μ-oxo of the $Cu_2^{II/III}$(O)(OH) intermediate, while its phenolate O-atom is oriented toward Cu_A (Fig. 5*A*). From 2O, a 2D scan for the concerted formation of the C-O and Cu_A-$O_{phenolate}$

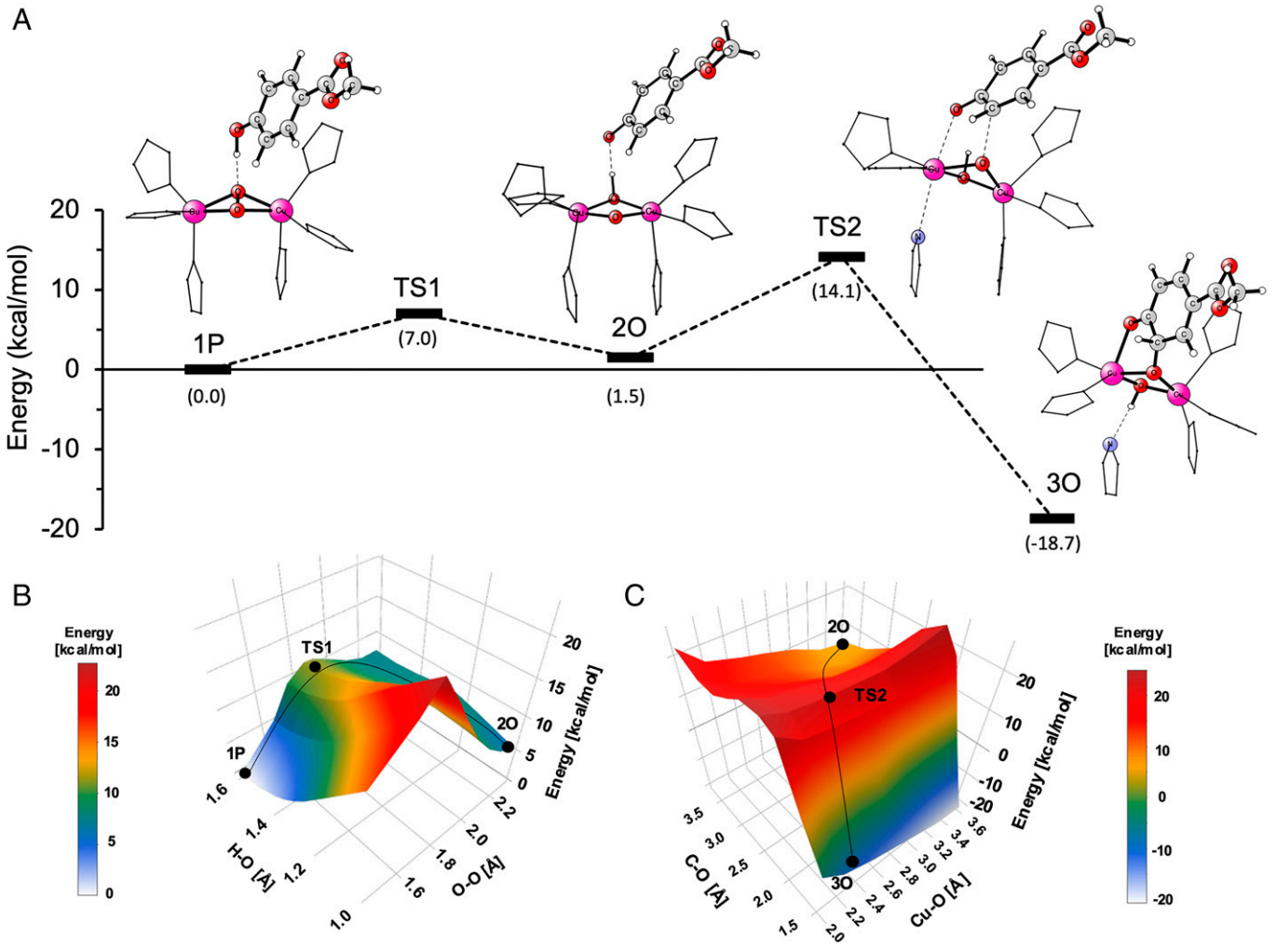

Fig. 4. Experimentally supported QM/MM mechanism of the key steps in the monooxygenase reaction of Ty. (*A*) The calculated reaction coordinate with energies and structures for the key intermediates and TSs. The Cu_2O_2 core and the bound 4-$COOCH_3$ substrate are shown as sticks, the first-coordination His residues are shown as lines, and all other atoms are omitted for clarity. Energies are calculated as single points upon the QM/MM-optimized geometries at the TPSS/def2-TZVPD level of theory in a homogeneous dielectric continuum with $\varepsilon_r = 8$. (*B* and *C*) The 2D scans for the two steps in the monooxygenation mechanism shown in *A* (reaction coordinates in *B* are $O_{peroxide}$-$H_{phenolic}$ and O-$O_{peroxide}$ and in *C* are C_{phenol}-$O_{\mu\text{-}oxo}$ and Cu_A-$O_{phenolate}$) performed at the QM/MM/TPSS/def2-SVP level of theory.

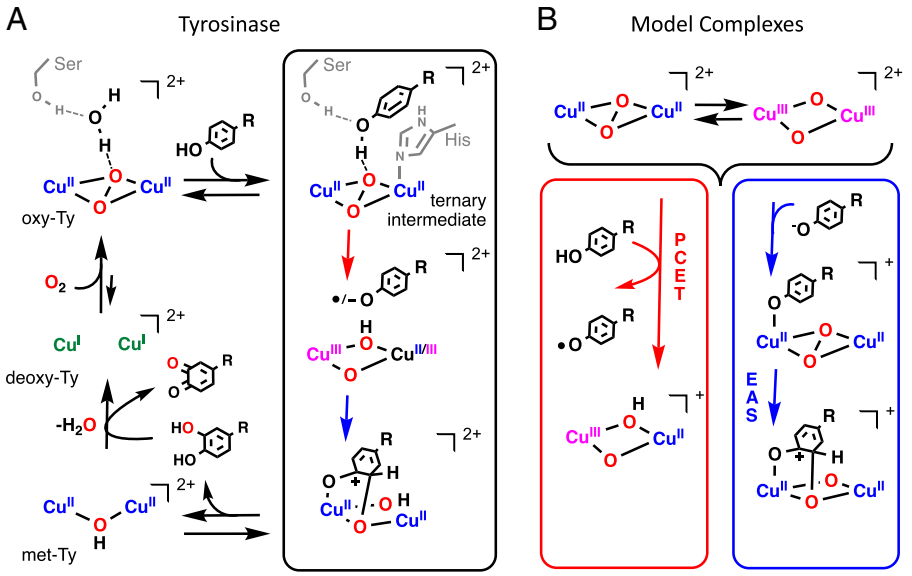

Fig. 5. Overview of the Cu_2O_2 chemistry in (*A*) Ty (from this study) and (*B*) model complexes.

bonds (Fig. 4*C*) shows a TS barrier of +14.1 kcal/mol to generate the thermodynamically favorable intermediate 3O (−18.7 kcal/mol), where the *ortho*-hydroxylated substrate is bridging the $Cu_2^{II}(OH)$ core (Fig. 4*A*). In this QM/MM-calculated mechanism, the TS (+14.1 kcal/mol) of the RLS is along the hydroxylation step, where the flexible $Cu_2^{II/III}(O)(OH)$ core moves toward the bound substrate to initiate the nonprotonated μ-oxo attack on the *ortho*-C concomitant with phenolate coordination to Cu_A. It should be noted that unlike previous proposals (24), the phenolic proton remains on the Cu_2O_2 core, as transfer to the nearby dissociated axial histidine of Cu_A is thermodynamically unfavorable along the entire monooxygenation reaction (*SI Appendix*, section 2.5.2). Our calculations also indicate that the native substrate, L-tyrosine, follows a very similar (kinetically and thermodynamically) monooxygenation reaction coordinate (*SI Appendix*, Fig. S19) to the one for the slow 4-$COOCH_3$ substrate (Fig. 5*A*).

The reaction coordinate in Fig. 5*A* was further evaluated by correlating the QM/MM-derived TS for the RLS with the experimental kinetic parameters obtained from the single-turnover monooxygenation reaction of oxy-Ty with 4-$COOCH_3$ from section 2.2. First, the experimental TS barrier of the RLS ($\Delta H^{\ddagger}_{exp}$ = +10.3 ±0.7 kcal/mol) is in reasonable agreement with the reaction coordinate in Fig. 4 ($\Delta E^{\ddagger}_{calc}$ = +14.1 kcal/mol, $\Delta H^{\ddagger}_{calc}$ = +11.4 kcal/mol) and is significantly lower than the corresponding barriers of other possible reaction coordinates (*SI Appendix*, section 2.5.1). Second, the experimentally observed small normal solvent KIE on k_2 (1.5 ± 0.1) is closely reproduced by QM-frequency calculations (calculated solvent KIE = 1.3; *SI Appendix*, *Materials and Methods*, section 1.2.7). Third, the lack of an experimentally observed inverse secondary KIE upon *ortho*-C-H/D substitution (1.05 ± 0.05) is in agreement with QM-frequency calculations (calculated secondary KIE = 1.0; *SI Appendix*, *Materials and Methods*, section 1.2.7) and is consistent with the small amount of sp^3 character of the *ortho*-C center in the structure of the TS of the RLS (TS2 in Fig. 4*A*). Together, our experimentally supported QM/MM calculations provide critical insights into the two key steps in the monooxygenation reaction mechanism of Ty, where the μ-η^2:η^2-peroxide O-O bond cleaves to accept the phenolic proton from the substrate, followed by coordination of the substrate phenolate to Cu_A concomitant with the *ortho*-hydroxylation of its aromatic ring by the nonprotonated μ-oxo of the $Cu_2(O)(OH)$ core.

3. Discussion

In this study, we have trapped and spectroscopically characterized the elusive catalytic ternary intermediate (Ty/O_2/monophenol) in the monooxygenation reaction of Ty. Correlation of our spectroscopic results to QM/MM calculations reveals the geometric and electronic structure of this ternary intermediate (1P in Fig. 3). The preservation of the μ-η^2:η^2-peroxide $Cu^{II}_2O_2$ core in this intermediate disproves previous proposals for conversion to a bis-μ-oxo $Cu^{III}_2O_2$ isomer upon substrate binding (20, 33). Importantly, the substrate binds fully protonated (i.e., as a monophenol) and forms an H bond to the μ-η^2:η^2-peroxide of the $Cu^{II}_2O_2$ core. Note that comparison of the active-site structure of 1P with that of the caddie protein bound to oxy-Ty (Protein Data Bank [PDB]: 1WX2) (34) reveals that the caddie residue Y98 is positioned similarly to the bound monophenol in 1P, and while not previously defined, it is likely to also be protonated and H-bonded to the μ-η^2:η^2-peroxide.

The substrate binding mode in 1P revises previous mechanistic proposals (21, 24, 35), all invoking a deprotonated monophenolate substrate directly coordinated to a Cu site, and thus, our study opens a framework for understanding the monooxygenation reactivity of Ty. First, our results provide an answer to the highly debated question regarding the identity of the proton acceptor site, where the candidates previously considered include 1) a second-sphere residue cluster (H_2O/Glu182/Asn191) (22), 2) one of the first-coordination sphere His residues (24), and 3) the $Cu^{II}_2O_2$ core to form a hydroperoxide (25, 36–38). Our results indicate that H^+ transfer to any of these active-site residues is not thermodynamically favorable (Table 1 and *SI Appendix*, section 2.5.2), and it is, in fact, the μ-η^2:η^2-peroxide that cleaves its O-O bond to accept the $H^{+/\bullet}$ from the bound substrate. This $H^{+/\bullet}$ transfer is facilitated by the direct H-bonding interaction between the μ-η^2:η^2-peroxide and the substrate hydroxyl group in 1P and is enabled by the attack of the Cu_2O_2 peroxide σ* unoccupied frontier molecular orbital on the highest occupied molecular orbital of the phenolic substrate (*SI Appendix*, Fig. S20). Second, the RLS of the monooxygenation reaction involves the concerted coordination of the monophenolate substrate to Cu_A with the formation of the C-O bond via the attack of the nonprotonated μ-oxo of the $Cu_2(O)(OH)$ core on the ortho-C of the substrate (Fig. 4*A*). During this step, Cu_A moves by

1.6 Å, dissociating from its axial histidine and coordinating the monophenolate substrate that is bound in the protein pocket, consistent with the plasticity of Cu_A observed in previous crystallographic studies (15, 24, 39).

The monooxygenation reaction mechanism defined in this study (Fig. 5*A*) accounts for the results of previous mechanistic studies of Ty and integrates the diverse reactivities of Cu_2O_2 model complexes toward monophenols or monophenolates within the biological context of the CBC enzymes. This study extends the facile interconversion between the μ-η^2:η^2-peroxide $Cu^{II}{}_2O_2$ and bis-μ-oxo $Cu^{III}{}_2O_2$ isomers (Fig. 5*B*, *Top*) (18) beyond model complexes to the Ty active site, where in the enzyme, this interconversion is coupled to $H^{+/\bullet}$ transfer from the bound substrate to the Cu_2O_2 core (Fig. 5*A*, red arrow). Note that $H^{\bullet}$ transfer to the μ-η^2:η^2-peroxide/bis-μ-oxo is also observed in the reaction of monophenols with $[Cu_2O_2]^{2+}$ model complexes (Fig. 5*B*, red box), which also exhibit small normal solvent KIE values (40). However, unlike model complexes, Ty provides protein pocket interactions that stabilize and orient the bound monophenolic substrate (Fig. 3) toward productive monooxygenation, rather than cage escape and phenoxyl radical coupling. The monophenolate coordination of the Cu center coupled to C-O bond formation in the RLS of the enzymatic monooxygenation reaction (Fig. 5*A*, blue arrow) is also observed in the reaction of Cu_2O_2 model complexes with monophenolate substrates (Fig. 5*B*, blue box) (20). However, in model complexes, this reaction step involves a Cu_2O_2 core with or without substrate coordination, while in Ty, it involves a protonated $Cu_2(O)(OH)$ species (Fig. 4).

An interesting consideration in the above reaction steps is the degree of concerted versus sequential two-electron transfer (ET) from the monophenolic substrate to the Cu_2O_2 core, leading to an electrophilic aromatic substitution (EAS) versus radical-coupling description, respectively. Our QM/MM calculations describe the monooxygenation mechanism as more sequential, where proton-coupled ET is followed by partial radical coupling (Fig. 4). Previous studies have argued for an EAS mechanism (28) based on the similarity of the Hammett linear free-energy dependence of the steady-state kinetic parameters for the reaction of Ty with monophenols ($\rho = -2.4$) with those for the EAS of monophenolates by μ-η^2:η^2-peroxide $Cu^{II}{}_2O_2$ model complexes ($\rho = -1.8$). However, we find that the Hammett plot for the steady-state kinetics is different from that for the pre–steady-state/single-turnover monooxygenation (*SI Appendix*, Fig. S21), which is up to $\times 10^3$ faster. Additional investigations are under way to determine the RLS step under steady-state conditions, as well as the concertedness of ET. Importantly, the insights from this study define the key reaction steps of the monooxygenation mechanism of Ty, where the O-O bond of the μ-η^2:η^2-peroxide Cu_2O_2 breaks to accept the phenolic $H^{+/\bullet}$, followed by attack of the nonprotonated μ-oxo on the *ortho*-C(sp^2) of the substrate, leading to formation of the Cu_A-O (phenolate) and C-O bonds via EAS/radical coupling (Fig. 5*A*).

Overall, by trapping the elusive catalytic ternary (Ty/O_2/monophenol) intermediate and defining its geometric and electronic structure, this study elucidates the key steps in the monooxygenation reaction of Ty. This mechanism unifies the diverse Cu_2O_2 model complex chemistry with the CBC enzymatic reactivity in biology. The mechanistic insights from this study are of broad fundamental interest in catalysis for controlled O_2 activation via incorporation of CBC sites into the ligand scaffolds of small model complexes or extended solids, such as the highly reactive Cu zeolites (41) and the highly modular metal-organic frameworks (42). Furthermore, the molecular-level description of the substrate-enzyme interactions for the RLS in melanin biosynthesis presents critical information for ongoing synthetic efforts toward designing effective Ty inhibitors (43) and Ty-activated prodrugs (44). More broadly, defining the mechanistic requirements of enzymatic monooxygenation serves as the key reference for correlating the diverse reactivities among other members of the CBC protein family, including CaOxs, which can oxidize *o*-catechols to *o*-quinones but lack monooxygenase reactivity, and the recently discovered *o*-aminophenol oxidases, which are able to monooxygenate both monophenols to catechols and *o*-aminophenols to *o*-nitrosophenols (3, 45, 46). Further mechanistic and spectroscopic investigations into the CaOx and hydroxyanilase reactions are under way to elucidate how nature controls O_2 activation and reactivity in CBC active sites.

Materials and Methods

The protein expression, purification, and redox-sensitive anaerobic preparation of Ty from *S. glaucescens*, as well as the computational protein model setup, were performed following the methodology we previously reported (26). SF-Abs spectra were collected using a SX.19 Applied Photophysics instrument placed in an anaerobic glovebox, and rR spectra were collected using 351-nm excitation (Innova Sabre Ar+ laser, 20 mW, 77 K). In the QM/MM calculations, the QM part employed density functional theory (mostly TPSS-D3 functional, recently calibrated in CBC model complexes) (47), the MM part employed the Amber ff14SB force field, and the standard hydrogen link-atom approach (subtractive scheme) with the electrostatic embedding was employed as the QM/MM coupling. Detailed information on reagents and instrumentation, experimental setups, sample preparations, and spectroscopic and computational QM/MM methods are provided in *SI Appendix, Materials and Methods*.

Data, Materials, and Software Availability. All study data are included in the article and/or supporting information, with cartesian coordinates for all computational models provided in Dataset S1.

ACKNOWLEDGMENTS. This research is supported by the National Institutes of Health (NIH, DK31450 to E.I.S.) and the Ministry of Education, Youth and Sports of the Czech Republic (MSMT CR, LTAUSA19148 to L.R.). Computer time at the IT4I supercomputer center was funded through the Ministry of Education, Youth and Sports of the Czech Republic (project e-INFRA CZ, ID 90140). P.C.A. acknowledges institutional support via the RVO86652036 project. We acknowledge Dr. Martin Srnec for his thoughtful guidance in the normal mode analysis and Dr. Wesley Transue for his assistance in the synthesis of the dideuterated 4-$COOCH_3$ substrate.

Author affiliations: [a]Department of Chemistry, Stanford University, Stanford, CA 94305; [b]Institute of Organic Chemistry and Biochemistry, Czech Academy of Sciences, 166 10, Prague 6, Czech Republic; [c]Faculty of Science, Charles University, 128 00 Prague 2, Czech Republic; and [d]Stanford Synchrotron Radiation Lightsource, SLAC National Accelerator Laboratory, Stanford University, Menlo Park, CA 94025

Author contributions: I.K., A.S., J.W.G., P.C.A., L.R., and E.I.S. designed research; I.K., A.S., J.W.G., and P.C.A. performed research; I.K., A.S., J.W.G., P.C.A., L.R., and E.I.S. analyzed data; and I.K., A.S., L.R., and E.I.S. wrote the paper.

1. K. Kirti, S. Amita, S. Priti, A. Mukesh Kumar, S. Jyoti, Colorful world of microbes: Carotenoids and their applications. *Adv. Biol.* **2014**, 1–13 (2014).
2. J. D. Simon, D. Peles, K. Wakamatsu, S. Ito, Current challenges in understanding melanogenesis: Bridging chemistry, biological control, morphology, and function. *Pigment Cell Melanoma Res.* **22**, 563–579 (2009).
3. E. I. Solomon *et al.*, Copper active sites in biology. *Chem. Rev.* **114**, 3659–3853 (2014).
4. J. D. Nosanchuk, A. Casadevall, The contribution of melanin to microbial pathogenesis. *Cell. Microbiol.* **5**, 203–223 (2003).
5. B. Ciui *et al.*, Wearable wireless tyrosinase bandage and microneedle sensors: Toward melanoma screening. *Adv. Healthc. Mater.* **7**, e1701264 (2018).
6. E. Buitrago *et al.*, Are human tyrosinase and related proteins suitable targets for melanoma therapy? *Curr. Top. Med. Chem.* **16**, 3033–3047 (2016).

7. I. Carballo-Carbajal *et al.*, Brain tyrosinase overexpression implicates age-dependent neuromelanin production in Parkinson's disease pathogenesis. *Nat. Commun.* **10**, 973 (2019).
8. N. Ananya, J. S. Kumar, S. H. Ram, L-DOPA, a promising pro-drug against Parkinson's disease: Present and future perspective. *Res. J. Biotechnol.* **14**, 10 (2019).
9. F. Tinello, A. Lante, Recent advances in controlling polyphenol oxidase activity of fruit and vegetable products. *Innov. Food Sci. Emerg. Technol.* **50**, 73–83 (2018).
10. M. J. Lobba *et al.*, Site-specific bioconjugation through enzyme-catalyzed tyrosine-cysteine bond formation. *ACS Cent. Sci.* **6**, 1564–1571 (2020).
11. A.-W. Struck *et al.*, An enzyme cascade for selective modification of tyrosine residues in structurally diverse peptides and proteins. *J. Am. Chem. Soc.* **138**, 3038–3045 (2016).
12. A. Frangu, K. Pravcová, P. Šilarová, T. Arbneshi, M. Sýs, Flow injection tyrosinase biosensor for direct determination of acetaminophen in human urine. *Anal. Bioanal. Chem.* **411**, 2415–2424 (2019).
13. M. Florescu, M. David, Tyrosinase-based biosensors for selective dopamine detection. *Sensors (Basel)* **17**, 1314 (2017).
14. K. Min, G. W. Park, Y. J. Yoo, J.-S. Lee, A perspective on the biotechnological applications of the versatile tyrosinase. *Bioresour. Technol.* **289**, 121730 (2019).
15. Y. Matoba, T. Kumagai, A. Yamamoto, H. Yoshitsu, M. Sugiyama, Crystallographic evidence that the dinuclear copper center of tyrosinase is flexible during catalysis. *J. Biol. Chem.* **281**, 8981–8990 (2006).
16. M. J. Baldwin *et al.*, Spectroscopic studies of side-on peroxide-bridged binuclear copper(II) model complexes of relevance to oxyhemocyanin and oxytyrosinase. *J. Am. Chem. Soc.* **114**, 10421–10431 (1992).
17. M. J. Baldwin *et al.*, Spectroscopic and theoretical studies of an end-on peroxide-bridged coupled binuclear copper(II) model complex of relevance to the active sites in hemocyanin and tyrosinase. *J. Am. Chem. Soc.* **113**, 8671–8679 (1991).
18. J. A. Halfen *et al.*, Reversible cleavage and formation of the dioxygen O-O bond within a dicopper complex. *Science* **271**, 1397–1400 (1996).
19. E. Pidcock, H. V. Obias, C. X. Zhang, K. D. Karlin, E. I. Solomon, Investigation of the reactive oxygen intermediate in an arene hydroxylation reaction performed by Xylyl-bridged binuclear copper complexes. *J. Am. Chem. Soc.* **120**, 7841–7847 (1998).
20. L. M. Mirica *et al.*, Tyrosinase reactivity in a model complex: An alternative hydroxylation mechanism. *Science* **308**, 1890–1892 (2005).
21. A. Spada, S. Palavicini, E. Monzani, L. Bubacco, L. Casella, Trapping tyrosinase key active intermediate under turnover. *Dalton Trans.* (33):6468–6471 (2009).
22. M. Goldfeder, M. Kanteev, S. Isaschar-Ovdat, N. Adir, A. Fishman, Determination of tyrosinase substrate-binding modes reveals mechanistic differences between type-3 copper proteins. *Nat. Commun.* **5**, 4505 (2014).
23. H. Decker, E. Solem, F. Tuczek, Are glutamate and asparagine necessary for tyrosinase activity of type-3 copper proteins? *Inorg. Chim. Acta* **481**, 32–37 (2018).
24. N. Fujieda *et al.*, Copper-oxygen dynamics in the tyrosinase mechanism. *Angew. Chem. Int. Ed. Engl.* **59**, 13385–13390 (2020).
25. J. S. Conrad, S. R. Dawso, E. R. Hubbard, T. E. Meyers, K. G. Strothkamp, Inhibitor binding to the binuclear active site of tyrosinase: Temperature, pH, and solvent deuterium isotope effects. *Biochemistry* **33**, 5739–5744 (1994).
26. Y. Matoba, K. Oda, Y. Muraki, T. Masuda, The basicity of an active-site water molecule discriminates between tyrosinase and catechol oxidase activity. *Int. J. Biol. Macromol.* **183**, 1861–1870 (2021).
27. I. Kipouros *et al.*, Evidence for H-bonding interactions to the μ-η^2:η^2-peroxide of oxy-tyrosinase that activate its coupled binuclear copper site. *Chem. Commun. (Camb.)* **58**, 3913–3916 (2022).
28. S. Yamazaki, S. Itoh, Kinetic evaluation of phenolase activity of tyrosinase using simplified catalytic reaction system. *J. Am. Chem. Soc.* **125**, 13034–13035 (2003).
29. J. N. Rodríguez-López, J. Tudela, R. Varón, F. García-Carmona, F. García-Cánovas, Analysis of a kinetic model for melanin biosynthesis pathway. *J. Biol. Chem.* **267**, 3801–3810 (1992).
30. B. T. Op't Holt *et al.*, Reaction coordinate of a functional model of tyrosinase: Spectroscopic and computational characterization. *J. Am. Chem. Soc.* **131**, 6421–6438 (2009).
31. N. C. Eickman, E. I. Solomon, J. A. Larrabee, T. G. Spiro, K. Lerch, Ultraviolet Resonance Raman Study of Oxytyrosinase. Comparison with Oxyhemocyanins. *J. Am. Chem. Soc.* **100**, 6429–6431 (1978).
32. E. Solem, F. Tuczek, H. Decker, Tyrosinase versus catechol oxidase: One asparagine makes the difference. *Angew. Chem. Int. Ed. Engl.* **55**, 2884–2888 (2016).
33. H. Decker, R. Dillinger, F. Tuczek, How Does Tyrosinase Work? Recent Insights from Model Chemistry and Structural Biology. *Angew. Chem. Int. Ed. Engl.* **39**, 1591–1595 (2000).
34. Y. Matoba *et al.*, Activation mechanism of the *Streptomyces* tyrosinase assisted by the caddie protein. *Biochemistry* **56**, 5593–5603 (2017).
35. D. E. Wilcox *et al.*, Substrate analog binding to the coupled binuclear copper active site in tyrosinase. *J. Am. Chem. Soc.* **107**, 4015–4027 (1985).
36. H. Jiang, W. Lai, Monophenolase and catecholase activity of *Aspergillus oryzae* catechol oxidase: Insights from hybrid QM/MM calculations. *Org. Biomol. Chem.* **18**, 5192–5202 (2020).
37. T. Lind, P. E. M. Siegbahn, R. H. Crabtree, A quantum chemical study of the mechanism of tyrosinase. *J. Phys. Chem. B* **103**, 1193–1202 (1999).
38. T. Inoue, Y. Shiota, K. Yoshizawa, Quantum chemical approach to the mechanism for the biological conversion of tyrosine to dopaquinone. *J. Am. Chem. Soc.* **130**, 16890–16897 (2008).
39. Y. Matoba *et al.*, Catalytic mechanism of the tyrosinase reaction toward the Tyr98 residue in the caddie protein. *PLoS Biol.* **16**, e3000077 (2018).
40. T. Osako *et al.*, Oxidation Mechanism of Phenols by Dicopper-Dioxygen (Cu_2/O_2) Complexes. *J. Am. Chem. Soc.* **125**, 11027–11033 (2003).
41. B. E. R. Snyder, M. L. Bols, R. A. Schoonheydt, B. F. Sels, E. I. Solomon, Iron and copper active sites in zeolites and their correlation to metalloenzymes. *Chem. Rev.* **118**, 2718–2768 (2018).
42. X. Feng *et al.*, Rational construction of an artificial binuclear copper monooxygenase in a metal-organic framework. *J. Am. Chem. Soc.* **143**, 1107–1118 (2021).
43. T.-S. Chang, An updated review of tyrosinase inhibitors. *Int. J. Mol. Sci.* **10**, 2440–2475 (2009).
44. M. Gabrielle *et al.*, Targeted prodrug design for the treatment of malignant melanoma. *J. Dermatol. Res. Ther.* **2**, 1–8 (2016).
45. J. W. Ginsbach *et al.*, Structure/function correlations among coupled binuclear copper proteins through spectroscopic and reactivity studies of NspF. *Proc. Natl. Acad. Sci. U.S.A.* **109**, 10793–10797 (2012).
46. A. Noguchi, T. Kitamura, H. Onaka, S. Horinouchi, Y. Ohnishi, A copper-containing oxidase catalyzes C-nitrosation in nitrosobenzamide biosynthesis. *Nat. Chem. Biol.* **6**, 641–643 (2010).
47. A. Stańczak, J. Chalupský, L. Rulíšek, M. Straka, Comprehensive theoretical view of the $[Cu_2\ O_2]$ side-on-peroxo-/bis-μ-oxo equilibria. *ChemPhysChem*, e202200076 (2022).